DRAFT
CMS Physics Analysis Summary

The content of this note is intended for CMS internal use and distribution only

Combined measurement and interpretation of differential Higgs boson production cross sections at $\sqrt{s}$=13 TeV

The CMS Collaboration

Abstract

The differential Higgs boson production cross sections are sensitive probes for new physics beyond the standard model. In particular, new physics may contribute in the gluon-gluon fusion loop, the dominant Higgs boson production mechanism at the LHC, and manifest itself as deviations from the expected standard model distributions. Combined spectra from the $H \rightarrow \gamma\gamma$, $H \rightarrow ZZ$ and $H \rightarrow b\bar{b}$ decay channels are presented, together with limits on the Higgs couplings using $35.9\,\mathrm{fb}^{-1}$ of proton-proton collision data recorded with the CMS detector at $\sqrt{s} = 13\,\mathrm{TeV}$.

1 Introduction

The Higgs boson, whose existence is predicted by the Brout-Englert-Higgs mechanism [1–3], is responsible for electroweak symmetry breaking in the standard model (SM). Since its discovery [4, 5] at the CERN LHC, extensive effort has been dedicated to the measurement of its properties and couplings.

In this analysis we study the differential cross sections for the production of Higgs bosons. Significant distortions of the shapes of differential cross sections appear when the Higgs couplings to quarks and to other bosons are varied. These distortions are particularly pronounced in the transverse momentum distribution. Measurements of differential distributions therefore provide information on the couplings that cannot be obtained from inclusive measurements [6–10]. By fitting parametrized predicted spectra to a state-of-the-art combination of differential cross sections, one can constrain Higgs couplings.

While the couplings to the top (y_t) and bottom (y_b) quarks are known with fair precision, there is still a relatively large uncertainty on the couplings to lighter quarks such as the charm. Increasing the precision on the Higgs boson couplings can provide fundamental insight into the SM, as they are free parameters in the SM Lagrangian and are sensitive to a range of beyond the SM theories [11, 12]. A proof-of-concept study determining limits on the modification of the Higgs coupling to the charm quark κ_c from the Higgs boson transverse momentum distribution was performed in Ref. [13] using $20.3\,\mathrm{fb}^{-1}$ of data collected by ATLAS at a centre-of-mass energy $\sqrt{s} = 8$ [14], yielding the overall bounds $\kappa_c \in [-16, 18]$. Direct detection of $H \to J/\psi$, which relies on charm-tagging, leads to significantly weaker limits: A recent study from the ATLAS Collaboration [15] quotes an expected upper limit on $\sigma(pp \to ZH) \times \mathrm{BR}(H \to cc)$ of 150^{+80}_{-40} times the SM value at 95% CL, which corresponds to a limit about 4 times weaker. An analysis by the ATLAS Collaboration of $H \to J/\psi\gamma$ [16], involving the detection of an associated photon, yields $|\kappa_c| < 429$ [17] at 95% CL. Limits from detection of $pp \to VH(\to cc)$ at LHCb [18] and $pp \to Hc$ [19] do not yield competitive limits at the current integrated luminosity, although projections to higher luminosities indicate they may do so in the future.

Both the ATLAS and CMS Collaborations have reported measurements of differential cross sections at $\sqrt{s} = 8$ and 13 TeV [20–29]. We report the measurements of differential cross sections obtained from a combination of results from the CMS Collaboration in the $H \to \gamma\gamma$ [30], $H \to ZZ \to 4\ell$ [27] and $H \to b\bar{b}$ [31] decay channels. The results of the individual decay channels were all obtained at $\sqrt{s} = 13$ TeV, using a data set corresponding to an integrated luminosity of about $35.9\,\mathrm{fb}^{-1}$. The differential cross sections for the following observables are combined: the Higgs boson transverse momentum p_T^H, the number of reconstructed hadronic jets N_jets, the Higgs boson rapidity $|y_\mathrm{H}|$, and the transverse momentum of the leading jet $p_\mathrm{T}^\mathrm{jet}$. Furthermore, we interpret the Higgs boson transverse momentum spectrum in terms of Higgs boson couplings. In order to take into account the many degrees of freedom offered by the Higgs coupling modifier framework [32], multiple couplings are varied simultaneously. We present results obtained by varying simultaneously (i) the modifier of the Higgs coupling to the charm quark κ_c and of the bottom quark κ_b, (ii) the modifier of the Higgs coupling to the top quark κ_t and the coefficient c_g of the anomalous direct coupling to the gluon in the heavy top mass limit, and (iii) κ_t and κ_b.

2 The CMS detector

The central feature of the CMS apparatus is a superconducting solenoid of 6 m internal diameter, providing a magnetic field of 3.8 T. Within the solenoid volume are a silicon pixel and strip

tracker, a lead tungstate crystal electromagnetic calorimeter (ECAL), and a brass and scintilla-tor hadron calorimeter (HCAL), each composed of a barrel and two endcap sections. Forward calorimeters extend the pseudorapidity coverage provided by the barrel and endcap detectors. Muons are detected in gas-ionization chambers embedded in the steel flux-return yoke outside the solenoid. In the barrel section of the ECAL, an energy resolution of about 1% is achieved for unconverted or late-converting photons in the tens of GeV energy range. The remaining barrel photons have a resolution of about 1.3% up to a pseudorapidity of $|\eta| = 1$, rising to about 2.5% at $|\eta| = 1.4$. In the endcaps, the resolution of unconverted or late-converting photons is about 2.5%, while the remaining endcap photons have a resolution between 3 and 4% [33]. When combining information from the entire detector, the jet energy resolution amounts typically to 15% at 10 GeV, 8% at 100 GeV, and 4% at 1 TeV, to be compared to about 40%, 12%, and 5% obtained when the ECAL and HCAL calorimeters alone are used. A more detailed description of the CMS detector, together with a definition of the coordinate system used and the relevant kinematic variables, can be found in Ref. [34].

3 Inputs to the combined analysis

For all the measurements used as input to the combination ($H \to \gamma\gamma$ [30], $H \to ZZ \to 4\ell$ [27] and boosted $H \to b\bar{b}$ [31]), the data set corresponds to an integrated luminosity of about 35.9 fb^{-1}. The $H \to b\bar{b}$ decay channel is only included in the combination of the Higgs bo-son transverse momentum spectrum, where it contributes to the measurements at the higher end of the spectrum ($p_T^H > 350$ GeV). It improves the precision in a region of phase space that is sensitive to effects that manifest themselves at high transverse momentum, and in which the data in the $H \to \gamma\gamma$ and $H \to ZZ$ decay channels are limited. Tables 1, 2, 3 and 4 show an overview of the bin boundaries used in the individual analyses.

The SM prediction for the differential cross sections is simulated at next-to-leading order (NLO) in perturbative quantum chromodynamics (QCD) with MADGRAPH5_aMC@NLO [35] for each of the four dominant Higgs production modes: gluon-gluon fusion (ggH), vector boson fusion (VBF), associated production with a W/Z boson (VH), and associated production with a top quark-antiquark pair (ttH). Up to two additional jets in association with the Higgs boson are included in the simulation. Simulated events are interfaced to PYTHIA [36] for parton shower-ing and hadronization and the CUETP8M1 [37] parameter set is applied to tune the underlying event. A weight is applied to simulated gluon fusion events to match the predictions from the NNLOPS program [38, 39]. This weight depends on the Higgs boson transverse momentum p_T^H and the number of jets in the event N_{jets}.

Each of the analyses used as input to the combination uses a different fiducial space. In the case of $H \to \gamma\gamma$, the fiducial phase space is defined by requiring the leading photon trans-verse momentum over the diphoton mass to be greater than 1/3 and the subleading photon transverse momentum over the diphoton mass to be greater than 1/4. Furthermore, for each photon candidate the sum of the generator level transverse energy of stable particles contained in a cone of radius $\Delta R = 0.3$ around the candidate is required to be less than 10 GeV, where ΔR is the angular separation between particles ($\Delta R = \sqrt{(\Delta\eta)^2 + (\Delta\phi)^2}$). In the case of $H \to ZZ$, the 4-lepton mass is required to be greater than 70 GeV, the leading Z-candidate mass must be greater than 40 GeV, leptons must be separated in angular space by at least $\Delta R > 0.02$. Further-more, at least two leptons must have a transverse momentum greater than 10 GeV and at least one greater than 20 GeV. In the case of $H \to b\bar{b}$, the analysis strategy requires the presence of a single anti-k_T jet with a cone size $R = 0.8$, $p_T > 450$ GeV, and $|\eta| < 2.5$. Soft and wide-angle radiation is removed using the soft drop mass algorithm [40][41]. The jet mass after application

of the soft drop mass algorithm m_{SD} peaks at the Higgs mass in the case of signal events. Cuts on the dimensionless mass scale variable for QCD jets $\rho = \log\left(m_{\mathrm{SD}}^2/p_{\mathrm{T}}^2\right)$ [40], which relates the jet transverse momentum to the jet mass, are used to avoid finite cone effects and the non-perturbative regime of the soft drop mass calculation. Events with isolated electrons, muons or taus with $p_{\mathrm{T}} > 10\,\mathrm{GeV}$ and $|y| < 2.5$ are vetoed in order to reduce the background from SM electroweak processes, and events with $E_{\mathrm{T}}^{\mathrm{miss}} > 140\,\mathrm{GeV}$ are vetoed in order to reduce the background from top-antitop quark production.

There are minor differences amongst the individual analyses in Refs. [27, 30, 31] and the inputs we used for the combination of differential observables. For $H \to \gamma\gamma$, an additional bin boundary in the $p_{\mathrm{T}}^{\mathrm{H}}$ spectrum is included at 600 GeV. For $H \to ZZ$, the bin boundaries in multiple spectra were modified to align them with those used in the $H \to \gamma\gamma$ analysis. Furthermore, the branching fractions of the two Z bosons to the various lepton configurations were fixed to their SM values, whereas in Ref. [27] these were allowed to float. For $H \to b\bar{b}$ the signal was split into two p_{T}-bins at generator level: the first with bin boundaries from 350 to 600 GeV and the second an overflow bin starting at 600 GeV, which aligns with the bin boundaries of the other decay channels. The original binning at reconstructed level is merged into two bins, with bin boundaries from 450 to 600 and 600 to 1000 GeV, chosen so that the majority of signal events in a reconstructed bin originate from one generator-level bin. The redefinition of the reconstructed transverse momentum categories necessitated a re-evaluation of the background model, which was performed using the same procedure as in the original analysis.

Channel	$p_{\mathrm{T}}^{\mathrm{H}}$ bin boundaries (GeV)								
$H \to \gamma\gamma$	[0, 15)	[15, 30)	[30, 45)	[45, 80)	[80, 120)	[120, 200)	[200, 350)	[350, 600)	[600, ∞)
$H \to ZZ$	[0, 15)	[15, 30)	[30, 80)		[80, 200)		[200, ∞)		
$H \to b\bar{b}$								[350, 600)	[600, ∞)

Table 1: $p_{\mathrm{T}}^{\mathrm{H}}$ bin boundaries for the $H \to \gamma\gamma$, $H \to ZZ$ and $H \to b\bar{b}$ decay channels.

Channel	N_{jets} bin boundaries (# of jets)				
$H \to \gamma\gamma$	0	1	2	3	≥ 4
$H \to ZZ$	0	1	2		≥ 3

Table 2: N_{jets} bins for the $H \to \gamma\gamma$ and the $H \to ZZ$ decay channels.

Channel	$|y_{\mathrm{H}}|$ bin boundaries					
$H \to \gamma\gamma$	[0.0, 0.15)	[0.15, 0.30)	[0.30, 0.60)	[0.60, 0.90)	[0.90, 2.50]	
$H \to ZZ$	[0.0, 0.15)	[0.15, 0.30)	[0.30, 0.60)	[0.60, 0.90)	[0.90, 1.20)	[1.20, 2.50]

Table 3: $|y_{\mathrm{H}}|$ bins for the $H \to \gamma\gamma$ and the $H \to ZZ$ decay channels.

Channel	$p_{\mathrm{T}}^{\mathrm{jet}}$ bin boundaries (GeV)					
$H \to \gamma\gamma$	[0, 30)	[30, 55)	[55, 95)	[95, 120)	[120, 200)	[200, ∞)
$H \to ZZ$	[0, 30)	[30, 55)	[55, 95)	[95, ∞)		

Table 4: $p_{\mathrm{T}}^{\mathrm{jet}}$ bin boundaries for the $H \to \gamma\gamma$ and the $H \to ZZ$ decay channels.

4 Statistical analysis

The cross sections are extracted through a simultaneous extended maximum likelihood fit [42] to the diphoton, four-lepton and the anti-k_T jet mass spectra in all the analysis categories of

$H \rightarrow \gamma\gamma$, $H \rightarrow ZZ$ and $H \rightarrow b\bar{b}$ respectively. Systematic uncertainties are implemented as nuisance parameters.

The number of expected signal events n^{sig} in a given reconstructed bin i, given analysis category k and given decay channel m is given by:

$$n_i^{\text{sig},km}(\vec{\Delta\sigma}|\vec{\theta}) = \sum_{j=1}^{n_b^{\text{gen}}} \Delta\sigma_j \cdot L(\vec{\theta}) \cdot A_j^{km}(\vec{\theta}) \cdot \text{BR}^m(\vec{\theta}) \cdot \varepsilon_{ji}^{km}(\vec{\theta}) + n_i^{\text{OOA},km}(\vec{\theta}) \,, \tag{1}$$

where:

- j is an index to bin j at generator level
- n_b^{gen} is the number of kinematic bins at generator level, which is the same for all decay channels
- $\vec{\Delta\sigma}$ is the set of differential cross sections at generator level, and L is the integrated luminosity of the samples used in this analysis.
- A_j^{km} is the acceptance (fraction of the overall cross section) in reconstructed bin j, and BR^m is the branching fraction of decay channel m.
- ε_{ji}^{km} is the efficiency with which events originating from bin j are reconstructed in bin i. Note that the corresponding matrix $\vec{\varepsilon}^{km}$ need not be square; the number of reconstructed bins may be smaller than the number of bins at generator level.
- $n_i^{\text{OOA},km}$ is the number of events originating from outside the fiducial phase space reconstructed in bin i, specific for category k and decay channel m. This contribution is roughly 1% of the total yield for $H \rightarrow \gamma\gamma$, and a negligible fraction for the other decay channels.
- $\vec{\theta}$ is the set of nuisance parameters.

The summation and the efficiencies ensure that bin-to-bin migrations are taken into account, effectively allowing unfolding of the detector effects. Following the prescription in Ref. [43], we found that no regularization term was needed.

An extended likelihood function [42] for a single decay channel m is constructed:

$$\mathcal{L}_m(\vec{\Delta\sigma}|\vec{\theta}) = \prod_{i=1}^{n_b^{\text{reco},m}} \prod_{k=1}^{n_{\text{cat}}^m} \prod_{l=1}^{n_{\mathcal{O}}^m} \left(\text{pdf}_i^{km}(\mathcal{O}_l^m|\vec{\Delta\sigma},\vec{\theta}) \right)^{N_{\text{obs}}^{iklm}} $$
$$\cdot \text{Poisson} \left(N_{\text{obs}}^{ikm} \,\middle|\, n_i^{\text{sig},km}(\vec{\Delta\sigma}|\vec{\theta}) + n_i^{\text{bkg},km}(\vec{\theta}) \right) \,, \tag{2}$$

where:

- $\mathcal{O}^m$ is the observable, i.e. the diphoton, four-lepton or the anti-k_T jet mass for the $H \rightarrow \gamma\gamma$, $H \rightarrow ZZ$ and $H \rightarrow b\bar{b}$ decay channels respectively,
- $n_b^{\text{reco},m}$ is the number of reconstructed bins, n_{cat}^m is the number of categories for the decay channel, and $n_{\mathcal{O}}^m$ is the number of bins for observable $\mathcal{O}$,
- N_{obs}^{iklm} is the number of observed events reconstructed in kinematic bin i, category k and observable bin l,
- $n_i^{\text{bkg},km}$ is the number of expected background events,
- $\text{pdf}_i^{km}(\mathcal{O}_l|\vec{\Delta\sigma},\vec{\theta})$ is the probability distribution function for the observable, based on the signal and background distributions of the observable.

In order to combine decay channels, the likelihood formulae for the individual decay channels are multiplied:

$$\mathcal{L}(\vec{\Delta\sigma}|\vec{\theta}) = \prod_{m=1}^{n_c} \mathcal{L}_m(\vec{\Delta\sigma}|\vec{\theta}) \cdot \mathrm{pdf}(\vec{\theta}),\tag{3}$$

where n_c is the number of decay channels included in the combination, $\mathcal{L}_m$ is the likelihood formula from Eq. 2 specific to decay channel m, and $\mathrm{pdf}(\vec{\theta})$ is the probability distribution of the nuisance parameters. For the individual analyses, the number of categories, invariant mass bins and even the number of reconstructed bins may differ, although the number of bins at generator level and their bin boundaries need to be aligned between decay channels. Note that a single set of differential cross sections and nuisance parameters is applied to all decay channels simultaneously.

The test statistic q is defined as:

$$q(\vec{\Delta\sigma}) = -2 \cdot \ln\left(\frac{\mathcal{L}\left(\vec{\Delta\sigma}\left|\hat{\hat{\vec{\theta}}}_{\vec{\Delta\sigma}}\right.\right)}{\mathcal{L}\left(\hat{\vec{\Delta\sigma}}\left|\hat{\vec{\theta}}\right.\right)} \right).\tag{4}$$

The quantities $\hat{\vec{\Delta\sigma}}$ and $\hat{\vec{\theta}}$ are the unconditional maximum likelihood estimates for the parameters $\vec{\Delta\sigma}$ and $\vec{\theta}$ respectively, while $\hat{\hat{\vec{\theta}}}_{\vec{\Delta\sigma}}$ denotes the maximum like estimate for $\vec{\theta}$ conditional on the values of $\vec{\Delta\sigma}$. It is assumed that q is χ^2-distributed.

The Higgs coupling modifiers are fitted through a largely analogous procedure, utilizing the full likelihood. The difference is that instead of freely floating parameters for the differential cross sections $\vec{\Delta\sigma}$, the differential cross sections are replaced with parametrizations of the theoretical spectra described in Sec. 5:

$$\vec{\Delta\sigma} \rightarrow \vec{\Delta\sigma}(\kappa_a, \kappa_b),\tag{5}$$

where κ_a and κ_b are the coupling modifiers to be fitted. The theoretical uncertainties described in Sec. 5 are implemented as nuisance parameters. The coupling modifiers are implemented as freely floating parameters in the fit, and as such the corresponding degree of freedom of q is equal to the number of coupling modifiers.

5 Theoretical predictions

Differential cross sections may be used constrain physical parameters. In the case of Higgs boson production through gluon fusion, finite quark mass effects and moderate variations to Higgs couplings may manifest in distortions of the p_T^H spectrum. We interpret the p_T^H spectrum for gluon fusion in terms of modifications of the couplings of the Higgs boson using two models: one tailored to heavy quarks and thus sensitive to effects at high p_T [44], and the other considering the effect of lighter quarks in the gluon fusion loop [13]. Higgs boson production in association with bottom and top quarks is taken to scale quadratically with κ_b and κ_t respectively. The other production processes are taken to be independent of these couplings. The coupling modifiers are described within the context of the kappa-framework [6, 32]:

$$\kappa_i^2 = \frac{y_i}{y_i^{\mathrm{SM}}},\tag{6}$$

where y_i is the Higgs boson coupling to particle i. The SM value of any κ_i is equal to 1.

162 Recent developments in transverse momentum resummation procedures have allowed more
163 accurate calculations of the p_T^H spectrum when including the effects of lighter quarks on Higgs
164 production through gluon fusion [45–48]. The p_T^H spectrum for gluon fusion has been calcu-
165 lated for simultaneous variations of κ_c and κ_b [13], providing a novel approach to constrain
166 these couplings via the p_T^H spectrum. The variations are computed in Ref. [13] and we pa-
167 rameterize these with a quadratic polynomial for each bin of the differential production cross
168 section, including an inhomogeneity due to the interference of the top quark with the bottom
169 and charm quarks. The Higgs coupling to the top quark is fixed to its SM value in this model.

170 A second model producing simultaneous variations of κ_t, c_g and κ_b by adding dimension-6
171 operators to the SM Lagrangian was built in Ref. [44]. This study employs an analytic resum-
172 mation performed up to next-to-next-to-leading logarithmic (NNLL) order for the lower p_T^H
173 region in order to obtain the p_T^H spectrum at NNLO+NNLL accuracy. The dimension-6 opera-
174 tor whose coefficient is c_g yields a direct coupling of the Higgs boson to the gluon, whose tensor
175 structure corresponds to the heavy top mass limit. The derivation of c_g is given in Ref. [44] and
176 the inclusive cross section is given by $\sigma \simeq \left|12c_g + \kappa_t\right|^2 \sigma^\mathrm{SM}$. Two other operators are included
177 to describe modifications of κ_t and κ_b. While the model allows simultaneous variation of all
178 three coupling modifiers, we consider only simultaneous variations of κ_t and c_g, and of κ_t and
179 κ_b. The precomputed spectra are taken as input from Ref. [44] and are parametrized using a
180 quadratic polynomial, neglecting the interference of the bottom and top quark in the gluon
181 fusion loop.

182 The coupling modifiers affect not only the production cross section of the Higgs boson, but its
183 branching fractions as well. Throughout our results we will consider the branching fractions
184 to be scaling with the Higgs coupling modifiers.

185 6 Systematic uncertainties

186 The systematic experimental uncertainties from the input analyses are incorporated in the com-
187 bination as nuisance parameters in the extended likelihood fit and are profiled. Among the de-
188 cay channels, correlations are taken into account for the systematic uncertainties in jet energy
189 scale and resolution, and integrated luminosity. Full descriptions of the experimental system-
190 atic uncertainties per decay channel may be found in Refs. [27, 30, 31].

191 Our measurement is made for the full phase space rather than limited to a fiducial phase space
192 (as is the case for the original $H \to \gamma\gamma$ and $H \to ZZ$ analyses). This means that uncertainties
193 in the acceptances for the individual analyses and in the branching fractions may affect our
194 results. The effect of the acceptance uncertainties per bin on the overall uncertainty is less
195 than one percent and so this is neglected in the combination. Likewise the overall effect of the
196 branching fraction uncertainties on the combined spectra is below one percent, and has been
197 neglected. The uncertainty in the inclusive production cross section from non-gluon fusion
198 production modes, determined to be about 2.1% [49], has been taken into account as a nuisance
199 parameter.

200 The theoretical predictions described in Sec. 5 are subject to theoretical uncertainties from the
201 renormalisation scale μ_R, the factorisation scale μ_F and the resummation scale Q. The stan-
202 dard approach to evaluate the impact of these uncertainties is to compute an envelope of scale
203 variations, and taking the extrema of the envelope. To this end, μ_R and μ_F are independently
204 varied between 0.5, 1 and 2 times their nominal value, whereas the fraction $\frac{\mu_R}{\mu_F}$ is not to be less
205 than 0.5 or greater than 2.0. As the theoretical spectra in the $\kappa_t/c_g/\kappa_b$ case and the κ_c/κ_b case
206 contain a resummation, the resummation scale Q is varied from 0.5 to 2 times its central value

207 (while keeping μ_F and μ_R at their central value). The theoretical uncertainties are determined
208 by applying the default approach of taking the minimum and maximum scale variations per
209 bin. The resulting uncertainties are shown in Table 5 for the κ_b/κ_c spectra and in Table 6 for the
210 κ_t/c_g spectra.

Bin boundaries (GeV)	[0, 15)	[15, 30)	[30, 45)	[45, 80)	[80, 120)
Δ^{scale} (%)	8.9%	6.6%	18.1%	22.0%	21.6%

Table 5: Theoretical uncertainties for the κ_b/κ_c spectra.

Bin boundaries (GeV)	[0, 15)	[15, 30)	[30, 45)	[45, 80)	[80, 120)	[120, 200)	[200, 350)	[350, 600)	[600, 800)
Δ^{scale} (%)	12.7%	7.4%	9.5%	12.8%	17.4%	19.3%	20.9%	23.4%	8.2%

Table 6: Theoretical uncertainties for the κ_t/c_g and κ_t/κ_b spectra.

Theoretical uncertainties are subject to bin-to-bin correlations, that are notoriously difficult to
calculate. We adopt a procedure that obtains a correlation coefficient directly from the individual scale variations [50]:

$$\rho = \frac{\sum_i (\sigma_{1,i} - \overline{\sigma}_1)(\sigma_{2,i} - \overline{\sigma}_2)}{\sqrt{\sum_i (\sigma_{1,i} - \overline{\sigma}_1)^2 \sum_i (\sigma_{2,i} - \overline{\sigma}_2)^2}} , \tag{7}$$

211 where $\sigma_{1(2),i}$ is the cross section in bin 1 (2) of the ith scale variation, $\overline{\sigma}_{1(2)}$ is the mean cross
212 section in bin 1 (2), and ρ is the resulting correlation coefficient between bin 1 and 2. The
213 correlation structure is characterized by strong correlations among the central bins. Only the
214 bins below 15 GeV and above 600 GeV in p_{T}^{H} are anti-correlated with the central region.

7 Results

7.1 Total cross section and BR$_{\gamma\gamma}$/BR$_{ZZ}$

217 The total cross section for Higgs production is measured to be 61.1 ± 6.0 (stat.) ± 3.7 (syst.) pb,
218 based on a combination of the total cross sections from $H \rightarrow \gamma\gamma$ (64.0 ± 9.6 pb) and $H \rightarrow ZZ$
219 (58.2 ± 9.8 pb). The likelihood scans for the individual decay channels and their combination
220 is shown in Fig. 1 (left). The combination result agrees with the current SM value of $55.6 \pm$
221 2.5 pb [49].

222 A measurement of the branching fraction of one decay channel is degenerate with a measure-
223 ment of the total cross section. However, the ratio of branching fractions for two decay channels
224 can be measured while profiling the total cross section. The ratio of the $H \rightarrow \gamma\gamma$ and $H \rightarrow ZZ$
225 branching fractions R is measured to be 0.092 ± 0.018 (stat.) ± 0.010 (syst.), based on a combi-
226 nation of $H \rightarrow \gamma\gamma$ and $H \rightarrow ZZ$. This is in agreement with the SM prediction of 0.086 [49].
227 The likelihood scan for R is shown in Fig. 1 (right).

7.2 Combinations of differential observables

229 The differential cross sections for the observables p_{T}^{H}, N_{jets}, $|y_{\text{H}}|$ and $p_{\text{T}}^{\text{jet}}$ are shown in Fig 2, 3,
230 4, and 5, including differential cross sections for Higgs production through gluon fusion for
231 the observable p_{T}^{H}. Corresponding bin-to-bin correlation matrices are given in Appendix A.
232 For the observables p_{T}^{H}, N_{jets} and $p_{\text{T}}^{\text{jet}}$, the last bin is an overflow bin; here the cross section
233 is given in pb, and is divided by the bin width of the second-to-last bin (ensuring that if the
234 integrated cross sections in the last and second-to-last bin are equal, the value in the histogram
235 is the same). Overall no significant deviations from the SM prediction are observed. For the p_{T}^{H}
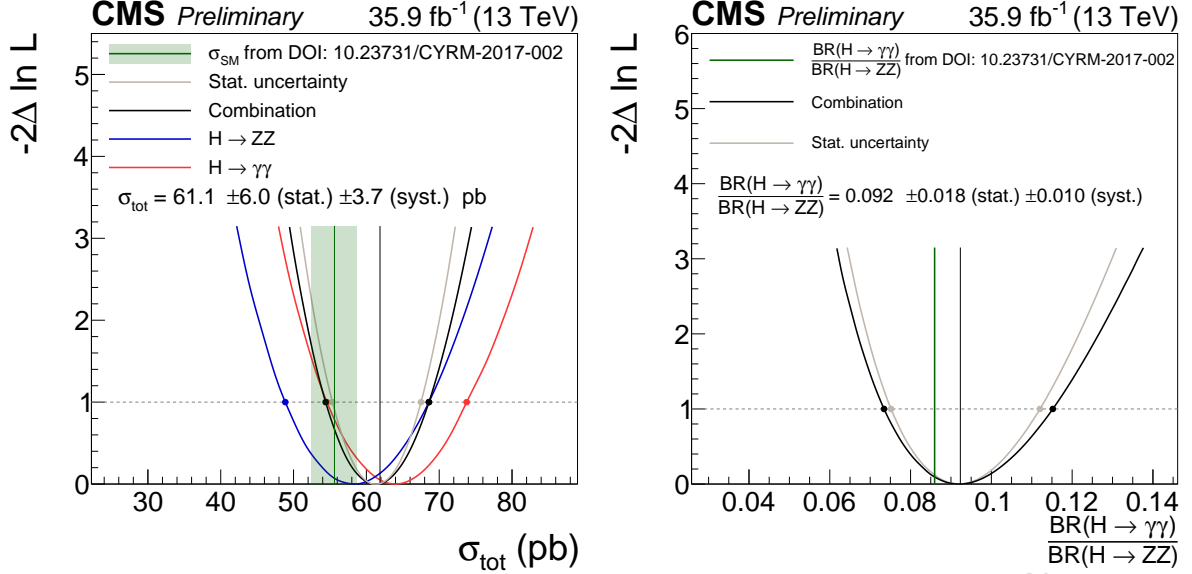
Figure 1: (left) Scan of the total cross section σ_{tot}, based on a combination of the total cross sections from $H \rightarrow \gamma\gamma$ ($64.0 \pm 9.6\,\text{pb}$) and $H \rightarrow ZZ$ ($58.2 \pm 9.8\,\text{pb}$. (right) Scan of the ratio of branching fractions R based on a combination of $H \rightarrow \gamma\gamma$ and $H \rightarrow ZZ$, while profiling all other parameters. The filled markers indicate the one standard deviation interval.

spectrum, the uncertainties are strongly statistically dominated; in particular, the systematic uncertainty is about half the statistical uncertainty in the last bin, and much smaller in all other bins. The uncertainty in the combination per bin varies between 30% and 40%. Relative to the spectrum of $H \rightarrow \gamma\gamma$ alone, the uncertainty decrease achieved by the combination is most notable in the lower p_T region. The contribution of $H \rightarrow b\bar{b}$ to the overall precision of the combination is strongest in the last p_T^H bin.

7.3   Fits of Higgs coupling modifiers: κ_b vs. κ_c

Figure 6(left) shows the one and two standard deviation contours of the fit of the κ_b/κ_c parametrization from Ref. [13] to data. The calculations from Ref. [13] are given up to the scale of the Higgs mass, and thus $H \rightarrow b\bar{b}$ (whose p_T^H spectrum starts at $p_T^H = 350\,\text{GeV}$) is not used as input for the results obtained here. The bin-to-bin correlations of the theoretical uncertainties are implemented as described in Sec. 6. The substructure on the combined scan shows a ring shape around the origin, and an almost one standard deviation agreement with the SM prediction.

In order to evaluate the effect of the shape on the constraints on κ_b and κ_c, the procedure is repeated with freely floating branching fractions, effectively removing constraints from the total width and from the overall normalization. The result of this fit is shown in Fig. 6(left). As expected, the range of allowed values of κ_b and κ_c is much wider than in the case of coupling-dependent branching fractions.

Separate limits can be set on κ_b and κ_c by profiling one coupling and scanning over the other. The results of these single-coupling scans are shown in Fig. 7 and Fig. 8. The observed uncertainties in the one-dimensional scans are:

$$-0.9 < \kappa_b < 0.9 \quad (-1.2 < \kappa_b < 1.2 \text{ expected}),$$
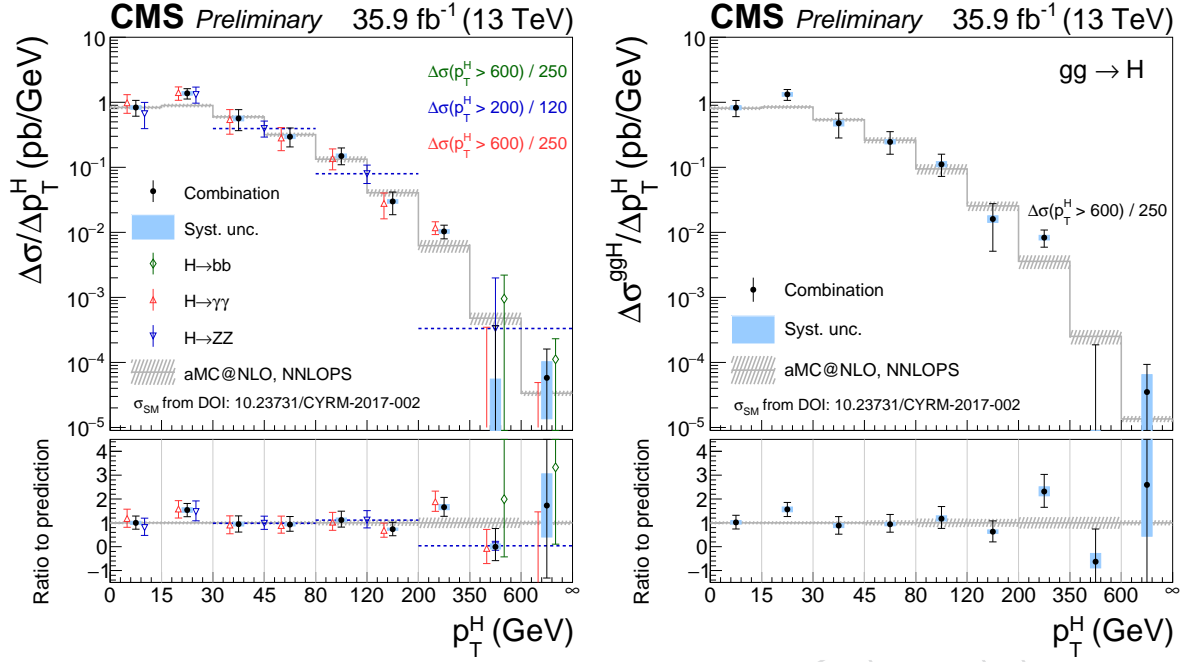$$-4.3 < \kappa_c < 4.3 \quad (-5.4 < \kappa_c < 5.3 \text{ expected}),$$

(8)

Figure 2: Best fit values and uncertainties of the cross sections and signal strengths. (left) p_T^H. (right) p_T^H while fixing non-gluon-fusion contributions to their SM expectation.
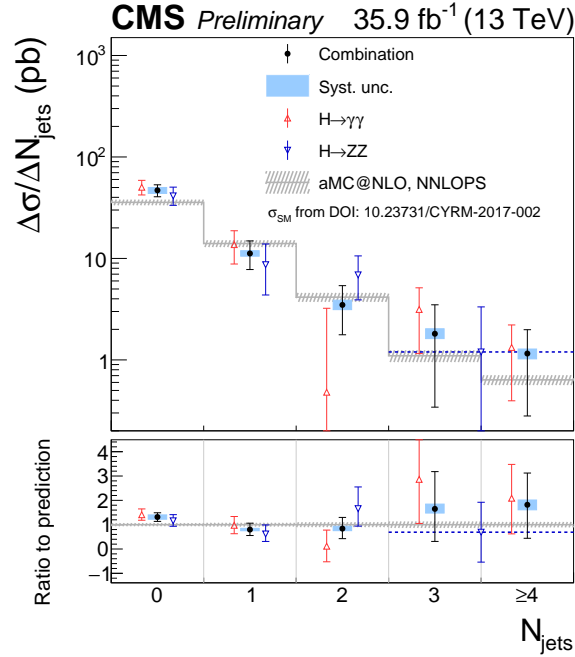

Figure 3: Best fit values and uncertainties of the cross sections and signal strengths for the N_{jets}-spectrum.
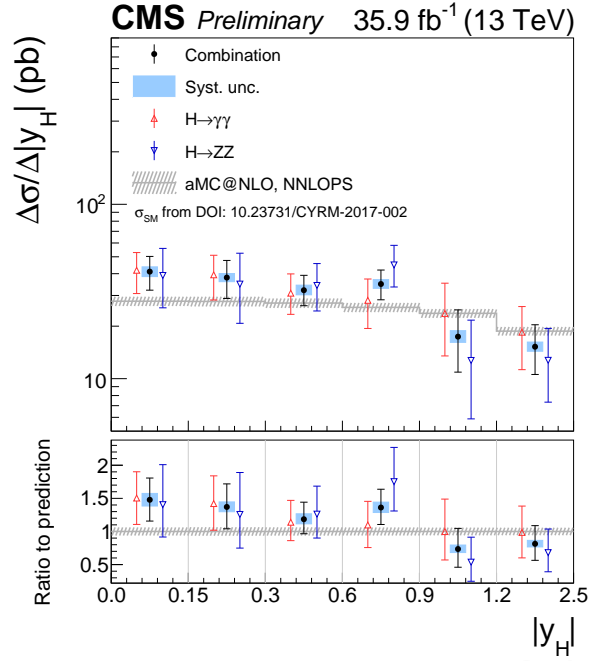
Figure 4: Expected best fit values and uncertainties of the cross sections and signal strengths for the $|y_H|$-spectrum.
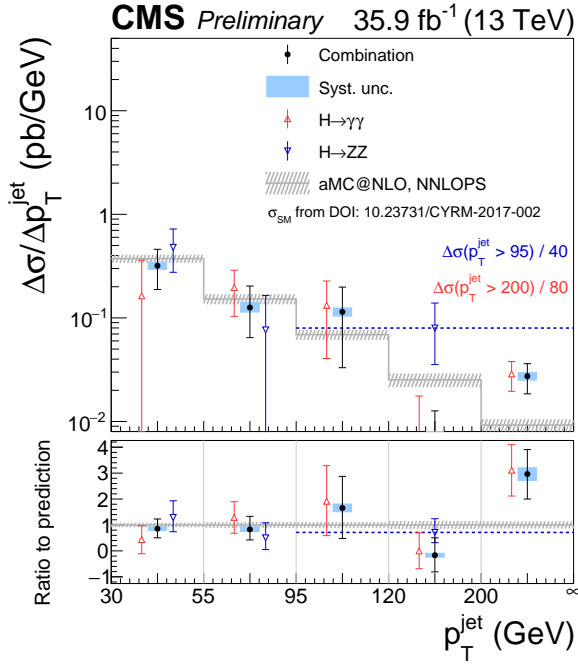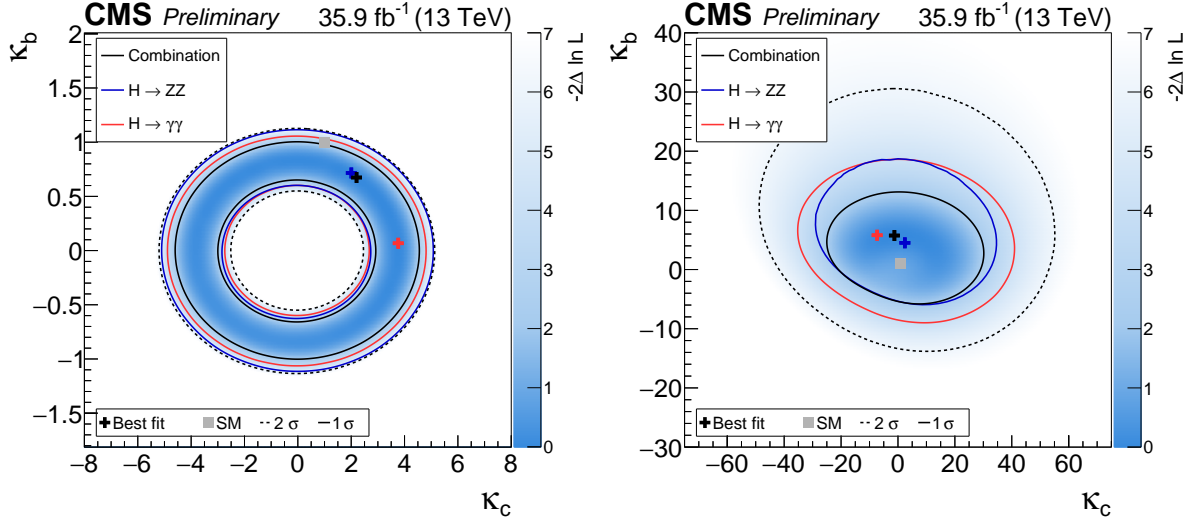

Figure 5: Expected best fit values and uncertainties of the cross sections and signal strengths for the p_T^{jet}-spectrum.

Figure 6: Simultaneous fit results for κ_b and κ_c. (left) One and two standard deviation contours are shown for the combined ($H \rightarrow \gamma\gamma$ and $H \rightarrow ZZ$) fit to data and for $H \rightarrow \gamma\gamma$ and $H \rightarrow ZZ$ separately, assuming a coupling dependency of the branching fractions. (right) One and two standard deviation contours are shown for the combined ($H \rightarrow \gamma\gamma$ and $H \rightarrow ZZ$) fit to data and for $H \rightarrow \gamma\gamma$ and $H \rightarrow ZZ$ separately, assuming freely floating branching fractions.

in the case of branching fractions that depend on κ_b and κ_c, and

$$-2.8 < \kappa_b < 9.9 \quad (-3.7 < \kappa_b < 7.3 \text{ expected}),$$
$$-18.0 < \kappa_c < 22.9 \quad (-15.7 < \kappa_c < 19.3 \text{ expected}), \tag{9}$$

in the case of freely floated branching fractions. For the coupling-dependent branching fractions, the results are shaped predominantly by constraints from the total width rather than by distortions of the p_T^H spectrum. If the branching fractions are fixed to their SM expectations, the one-dimensional scans yield the following expected uncertainties:

$$-1.9 < \kappa_b < 2.9 \quad (\text{expected}),$$
$$-8.7 < \kappa_c < 10.6 \quad (\text{expected}). \tag{10}$$

These limits are comparable to those in Ref. [13], where $\kappa_c \in [-16, 18]$, noting that the results here are based on a larger data set. The limits obtained are competitive with the limits from other direct search channels summarized in Sec. 1.

7.4 Fits of Higgs coupling modifiers: κ_t vs. c_g and κ_t vs. κ_b

The fits are repeated in a way analogous to that of Sec. 7.3 but with κ_t, c_g and κ_b as the parameters of the fit, using the parametrization obtained from Ref. [44]. The combined log-likelihood scan for κ_t vs. c_g, assuming branching fractions that depend on the couplings, is shown in Fig. 9(left). The normalization of the spectrum is, by construction, equal to the SM normalization for the points ($\kappa_t = 1.0, c_g = 0.0$) and ($\kappa_t = 0.0, c_g \simeq 0.08$). The differential shape of the parametrization s is calculated by normalizing the differential cross section to one:

$$s_i(\kappa_t, c_g) = \frac{\sigma_i(\kappa_t, c_g)}{\sum_j \sigma_j(\kappa_t, c_g)}, \tag{11}$$
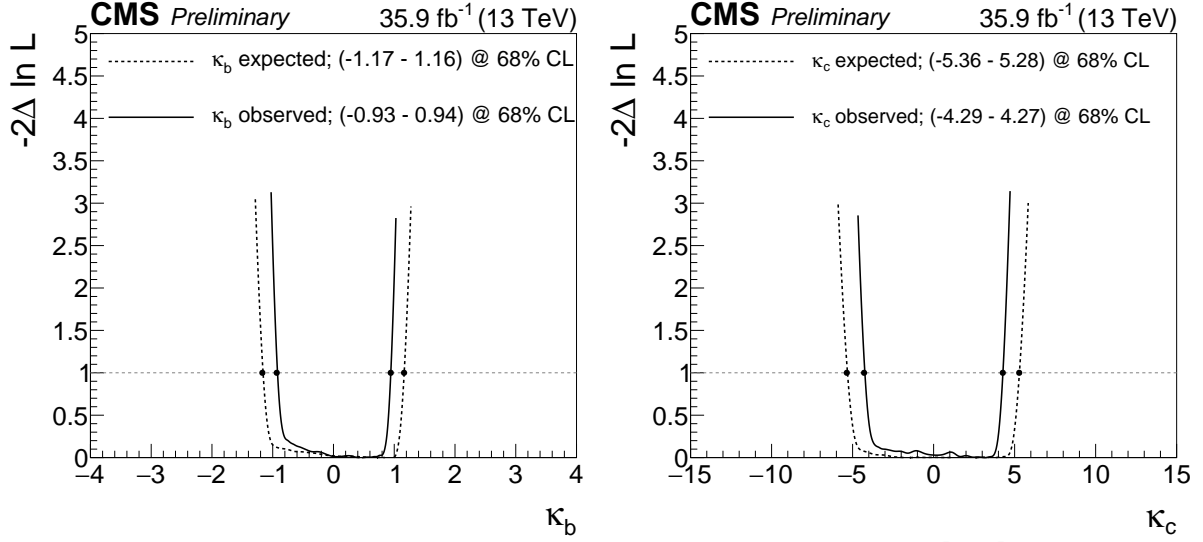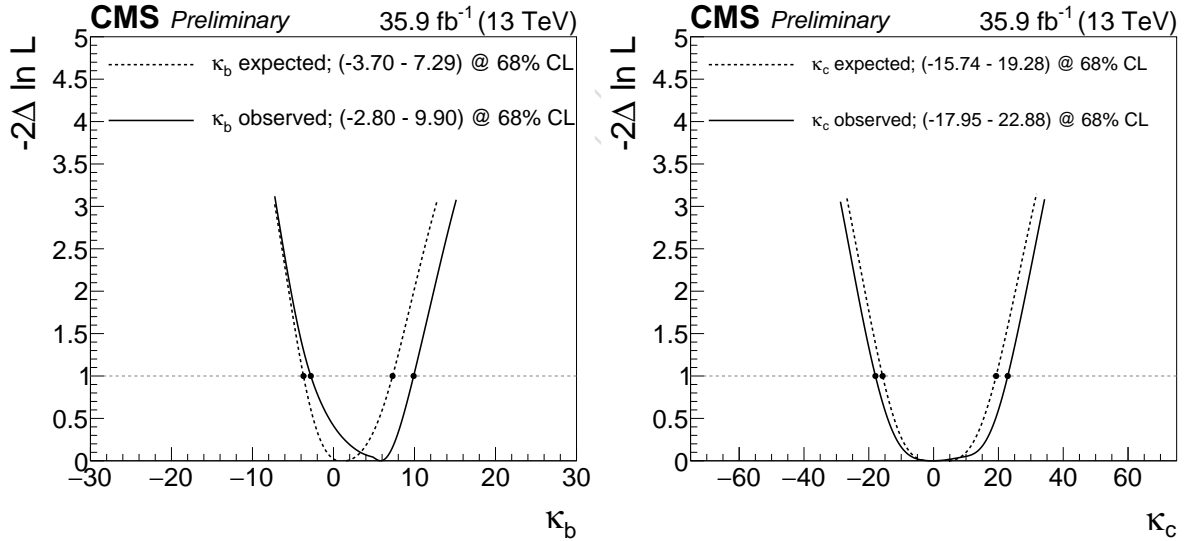
Figure 7: Scans of only one coupling, while profiling the other. The filled markers indicate the one standard deviation interval. The branching fractions were considered dependent on the values of the couplings. (left) Scan of κ_b while profiling κ_c. (right) Scan of κ_c while profiling κ_b.

Figure 8: Scans of only one coupling, while profiling the other. The filled markers indicate the one standard deviation interval. The branching fractions were freely floated in the fit. (left) Scan of κ_b while profiling κ_c. (right) Scan of κ_c while profiling κ_b.

where σ_i is the parametrization in bin i. Further simplification reveals that the shape of the parametrization for κ_t/c_g variations becomes a function of the ratio of the two couplings, $s_i\left(\frac{\kappa_t}{c_g}\right)$. Thus any discrimination power in the radial direction with respect to the origin stems from constraints on the overall normalization, whereas discrimination in the angular direction stems from constraints on the shape of the distribution. The angular dependence of the log-likelihood function becomes apparent in Fig. 9(right), where the branching fractions were freely floated in the fit. Except at small values of the couplings, the constraint on the couplings depends on their ratio. The two symmetric sets of contours are due to a symmetry of the parametrization under $(\kappa_t, c_g) \rightarrow (-\kappa_t, -c_g)$.
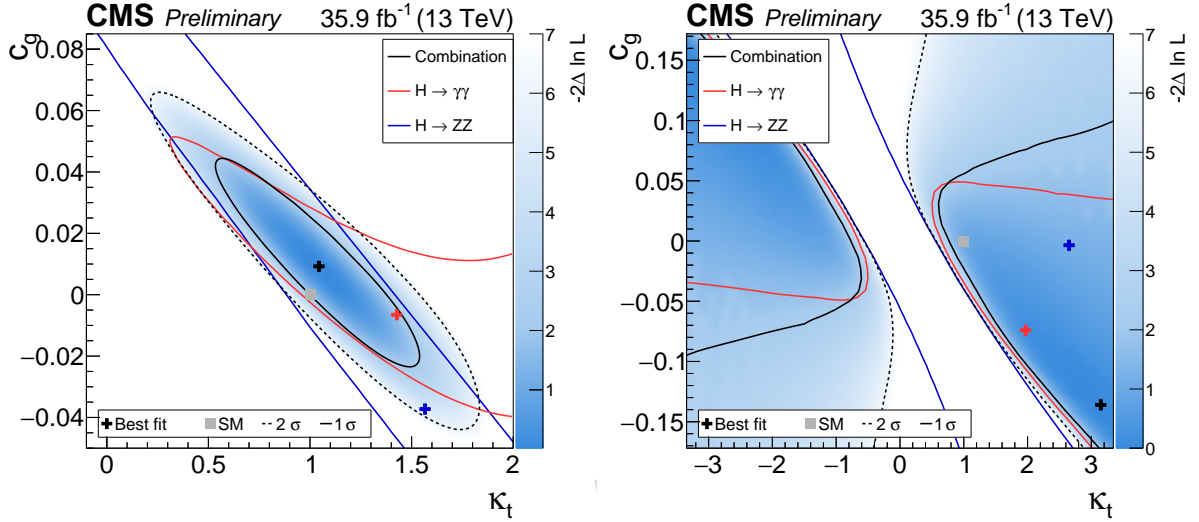

Figure 9: Simultaneous fit results for κ_t and c_g. (left) One and two standard deviation contours are shown for the combined ($H \rightarrow \gamma\gamma$, $H \rightarrow ZZ$ and $H \rightarrow b\bar{b}$) fit to data and for $H \rightarrow \gamma\gamma$ and $H \rightarrow ZZ$ separately, assuming a coupling dependency of the branching fractions. (right) One and two standard deviation contours are shown for the combined ($H \rightarrow \gamma\gamma$, $H \rightarrow ZZ$ and $H \rightarrow b\bar{b}$) fit to data and for $H \rightarrow \gamma\gamma$ and $H \rightarrow ZZ$ separately, assuming freely floating branching fractions.

Figure 10(left) shows the combined log-likelihood scan as a function of κ_t and κ_b, with branching fractions scaling appropriately with the coupling modifiers and Figure 10(right) with freely floating branching fractions. As the $H \rightarrow \gamma\gamma$ branching fraction depends linearly on κ_t, the constraints on $H \rightarrow \gamma\gamma$ and the combination in Figure 10(left) are not symmetric with respect to the κ_t-axis. For freely floating branching fractions, the parametrization is symmetric under $(\kappa_t, \kappa_b) \rightarrow (-\kappa_t, -\kappa_b)$, which explains the observed symmetry in in Figure 10(right).

8 Conclusion

A combination of differential cross sections for the differential observables p_T^H, N_{jets}, $|y_H|$ and p_T^{jet} has been presented, using 35.9 fb^{-1} of proton-proton collision data obtained at $\sqrt{s} = 13$ TeV with the CMS detector. The spectra obtained are based on data from the $H \rightarrow \gamma\gamma$, $H \rightarrow ZZ$ and $H \rightarrow b\bar{b}$ decay channels. The overall uncertainty is decreased by 15% relative to that for $H \rightarrow \gamma\gamma$ alone by combining the p_T^H spectra. The decrease is larger in the lower p_T^H region than in the high p_T^H tails. No significant deviations from the SM are observed in any differential distribution.
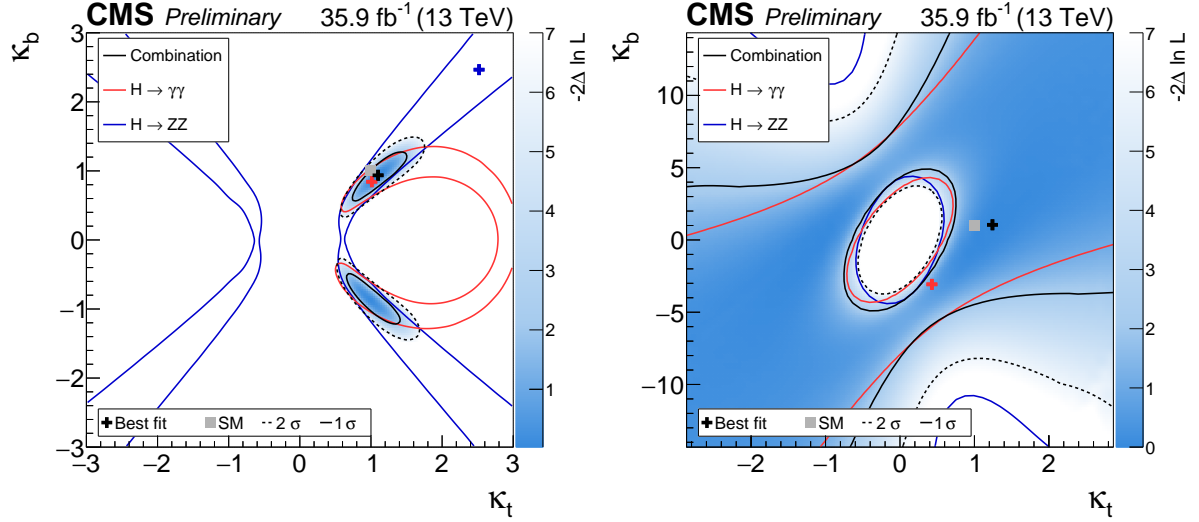
Figure 10: Simultaneous combined fit results for κ_t and κ_b. (left) One and two standard deviation contours are shown for the combined ($H \to \gamma\gamma$, $H \to ZZ$ and $H \to b\bar{b}$) fit to data and for $H \to \gamma\gamma$ and $H \to ZZ$ separately, assuming a coupling dependency of the branching fractions. (right) One and two standard deviation contours are shown for the combined ($H \to \gamma\gamma$, $H \to ZZ$ and $H \to b\bar{b}$) fit to data and for $H \to \gamma\gamma$ and $H \to ZZ$ separately, where the branching fractions were freely floated in the fit.

281 The spectra obtained were interpreted in the Higgs coupling modifier framework, in which
282 simultaneous variations of κ_b and κ_c, κ_t and κ_g and κ_t and κ_b were fitted to the combination
283 of the p_T^H-spectrum. The limits obtained on individual couplings were $-0.9 < \kappa_b < 0.9$ and
284 $-4.3 < \kappa_c < 4.3$, assuming the branching fractions scale with the coupling modifiers. For
285 the charm coupling κ_c in particular, this measurement is competitive with those obtained from
286 direct searches.

287 References

288 [1] P. W. Higgs, "Broken Symmetries and the Masses of Gauge Bosons", *Phys. Rev. Lett.* **13**
289 (1964) 508–509, `doi:10.1103/PhysRevLett.13.508`. [,160(1964)].

290 [2] F. Englert and R. Brout, "Broken Symmetry and the Mass of Gauge Vector Mesons",
291 *Phys. Rev. Lett.* **13** (1964) 321–323, `doi:10.1103/PhysRevLett.13.321`. [,157(1964)].

292 [3] G. S. Guralnik, C. R. Hagen, and T. W. B. Kibble, "Global Conservation Laws and
293 Massless Particles", *Phys. Rev. Lett.* **13** (1964) 585–587,
294 `doi:10.1103/PhysRevLett.13.585`. [,162(1964)].

295 [4] ATLAS Collaboration, "Observation of a new particle in the search for the Standard
296 Model Higgs boson with the ATLAS detector at the LHC", *Phys. Lett.* **B716** (2012) 1–29,
297 `doi:10.1016/j.physletb.2012.08.020`, `arXiv:1207.7214`.

298 [5] CMS Collaboration, "Observation of a new boson at a mass of 125 GeV with the CMS
299 experiment at the LHC", *Phys. Lett.* **B716** (2012) 30–61,
300 `doi:10.1016/j.physletb.2012.08.021`, `arXiv:1207.7235`.

[6] ATLAS, CMS Collaboration, "Measurements of the Higgs boson production and decay rates and constraints on its couplings from a combined ATLAS and CMS analysis of the LHC pp collision data at $\sqrt{s} = 7$ and 8 TeV", *JHEP* **08** (2016) 045, `doi:10.1007/JHEP08(2016)045`, `arXiv:1606.02266`.

[7] ATLAS Collaboration, "Measurements of the Higgs boson production and decay rates and coupling strengths using pp collision data at $\sqrt{s} = 7$ and 8 TeV in the ATLAS experiment", *Eur. Phys. J.* **C76** (2016), no. 1, 6, `doi:10.1140/epjc/s10052-015-3769-y`, `arXiv:1507.04548`.

[8] CMS Collaboration, "Precise determination of the mass of the Higgs boson and tests of compatibility of its couplings with the standard model predictions using proton collisions at 7 and 8 TeV", *Eur. Phys. J.* **C75** (2015), no. 5, 212, `doi:10.1140/epjc/s10052-015-3351-7`, `arXiv:1412.8662`.

[9] ATLAS Collaboration, "Combined measurements of Higgs boson production and decay in the $H \to ZZ^* \to 4\ell$ and $H \to \gamma\gamma$ channels using $\sqrt{s} = 13$ TeV pp collision data collected with the ATLAS experiment", ATLAS Conference Note ATLAS-CONF-2017-047, 2017.

[10] CMS Collaboration, "Combined measurements of the Higgs boson's couplings at $\sqrt{s} = 13$ TeV", CMS Physics Analysis Summary CMS-PAS-HIG-17-031, 2018.

[11] S. Dimopoulos and H. Georgi, "Softly Broken Supersymmetry and SU(5)", *Nucl. Phys.* **B193** (1981) 150–162, `doi:10.1016/0550-3213(81)90522-8`.

[12] E. Witten, "Dynamical Breaking of Supersymmetry", *Nucl. Phys.* **B188** (1981) 513, `doi:10.1016/0550-3213(81)90006-7`.

[13] F. Bishara, U. Haisch, P. F. Monni, and E. Re, "Constraining Light-Quark Yukawa Couplings from Higgs Distributions", *Phys. Rev. Lett.* **118** (2017), no. 12, 121801, `doi:10.1103/PhysRevLett.118.121801`, `arXiv:1606.09253`.

[14] ATLAS Collaboration, "Measurements of the Total and Differential Higgs Boson Production Cross Sections Combining the $H \to \gamma\gamma$ and $H \to ZZ \to 4\ell$ Decay Channels at $\sqrt{s}$=8 TeV with the ATLAS Detector", *Phys. Rev. Lett.* **115** (2015), no. 9, 091801, `doi:10.1103/PhysRevLett.115.091801`, `arXiv:1504.05833`.

[15] ATLAS Collaboration, "Search for the Decay of the Higgs Boson to Charm Quarks with the ATLAS Experiment", `arXiv:1802.04329`.

[16] ATLAS Collaboration, "Search for Higgs and Z Boson Decays to $J/\psi\gamma$ and $Y(nS)\gamma$ with the ATLAS Detector", *Phys. Rev. Lett.* **114** (2015), no. 12, 121801, `doi:10.1103/PhysRevLett.114.121801`, `arXiv:1501.03276`.

[17] M. König and M. Neubert, "Exclusive Radiative Higgs Decays as Probes of Light-Quark Yukawa Couplings", *JHEP* **08** (2015) 012, `doi:10.1007/JHEP08(2015)012`, `arXiv:1505.03870`.

[18] LHCb Collaboration, "Search for $H^0 \to b\bar{b}$ or $c\bar{c}$ in association with a W or Z boson in the forward region of pp collisions", LHCb Conference Note, 2016.

[19] I. Brivio, F. Goertz, and G. Isidori, "Probing the Charm Quark Yukawa Coupling in Higgs+Charm Production", *Phys. Rev. Lett.* **115** (2015), no. 21, 211801, `doi:10.1103/PhysRevLett.115.211801`, `arXiv:1507.02916`.

[20] ATLAS Collaboration, "Measurements of fiducial and differential cross sections for Higgs boson production in the diphoton decay channel at $\sqrt{s} = 8$ TeV with ATLAS", *JHEP* **09** (2014) 112, doi:10.1007/JHEP09(2014)112, arXiv:1407.4222.

[21] CMS Collaboration, "Measurement of differential cross sections for Higgs boson production in the diphoton decay channel in pp collisions at $\sqrt{s} = 8$ TeV", *Eur. Phys. J.* **C76** (2016), no. 1, 13, doi:10.1140/epjc/s10052-015-3853-3, arXiv:1508.07819.

[22] ATLAS Collaboration, "Fiducial and differential cross sections of Higgs boson production measured in the four-lepton decay channel in pp collisions at $\sqrt{s}$=8 TeV with the ATLAS detector", *Phys. Lett.* **B738** (2014) 234–253, doi:10.1016/j.physletb.2014.09.054, arXiv:1408.3226.

[23] CMS Collaboration, "Measurement of differential and integrated fiducial cross sections for Higgs boson production in the four-lepton decay channel in pp collisions at $\sqrt{s} = 7$ and 8 TeV", *JHEP* **04** (2016) 005, doi:10.1007/JHEP04(2016)005, arXiv:1512.08377.

[24] ATLAS Collaboration, "Measurement of fiducial differential cross sections of gluon-fusion production of Higgs bosons decaying to $WW^* \to e\nu\mu\nu$ with the ATLAS detector at $\sqrt{s} = 8$ TeV", *JHEP* **08** (2016) 104, doi:10.1007/JHEP08(2016)104, arXiv:1604.02997.

[25] CMS Collaboration, "Measurement of the transverse momentum spectrum of the Higgs boson produced in pp collisions at $\sqrt{s} = 8$ TeV using $H \to WW$ decays", *JHEP* **03** (2017) 032, doi:10.1007/JHEP03(2017)032, arXiv:1606.01522.

[26] ATLAS Collaboration, "Measurement of inclusive and differential cross sections in the $H \to ZZ^* \to 4\ell$ decay channel in pp collisions at $\sqrt{s} = 13$ TeV with the ATLAS detector", *JHEP* **10** (2017) 132, doi:10.1007/JHEP10(2017)132, arXiv:1708.02810.

[27] CMS Collaboration, "Measurements of properties of the Higgs boson decaying into the four-lepton final state in pp collisions at $\sqrt{s} = 13$ TeV", *JHEP* **11** (2017) 047, doi:10.1007/JHEP11(2017)047, arXiv:1706.09936.

[28] ATLAS Collaboration, "Combined measurement of differential and total cross sections in the $H \to \gamma\gamma$ and the $H \to ZZ^* \to 4\ell$ decay channels at $\sqrt{s} = 13$ TeV with the ATLAS detector", arXiv:1805.10197. Submitted to *Phys. Lett. B*.

[29] ATLAS Collaboration, "Measurements of Higgs boson properties in the diphoton decay channel with 36 fb^{-1} of pp collision data at $\sqrt{s} = 13$ TeV with the ATLAS detector", arXiv:1802.04146.

[30] CMS Collaboration, "Measurement of differential fiducial cross sections for Higgs boson production in the diphoton decay channel in pp collisions at $\sqrt{s} = 13$ TeV", CMS Physics Analysis Summary CMS-PAS-HIG-17-015, 2017.

[31] CMS Collaboration, "Inclusive search for a highly boosted Higgs boson decaying to a bottom quark-antiquark pair", *Phys. Rev. Lett.* **120** (2018), no. 7, 071802, doi:10.1103/PhysRevLett.120.071802, arXiv:1709.05543.

[32] LHC Higgs Cross Section Working Group Collaboration, "LHC HXSWG interim recommendations to explore the coupling structure of a Higgs-like particle", arXiv:1209.0040.

[33] CMS Collaboration, "Performance of photon reconstruction and identification with the CMS detector in proton-proton collisions at $\sqrt{s} = 8\,\text{TeV}$", *JINST* **10** (2015) P08010, doi:10.1088/1748-0221/10/08/P08010, arXiv:1502.02702.

[34] CMS Collaboration, "The CMS experiment at the CERN LHC", *JINST* **3** (2008) S08004, doi:10.1088/1748-0221/3/08/S08004.

[35] J. Alwall et al., "The automated computation of tree-level and next-to-leading order differential cross sections, and their matching to parton shower simulations", *JHEP* **07** (2014) 079, doi:10.1007/JHEP07(2014)079, arXiv:1405.0301.

[36] T. Sjöstrand et al., "An Introduction to PYTHIA 8.2", *Comput. Phys. Commun.* **191** (2015) 159–177, doi:10.1016/j.cpc.2015.01.024, arXiv:1410.3012.

[37] P. Skands, S. Carrazza, and J. Rojo, "Tuning PYTHIA 8.1: the Monash 2013 Tune", *Eur. Phys. J. C* **74** (Apr, 2014) 3024. 57 p. Comments: 57 pages.

[38] K. Hamilton, P. Nason, and G. Zanderighi, "MINLO: Multi-Scale Improved NLO", *JHEP* **10** (2012) 155, doi:10.1007/JHEP10(2012)155, arXiv:1206.3572.

[39] A. Kardos, P. Nason, and C. Oleari, "Three-jet production in POWHEG", *JHEP* **04** (2014) 043, doi:10.1007/JHEP04(2014)043, arXiv:1402.4001.

[40] M. Dasgupta, A. Fregoso, S. Marzani, and G. P. Salam, "Towards an understanding of jet substructure", *JHEP* **09** (2013) 029, doi:10.1007/JHEP09(2013)029, arXiv:1307.0007.

[41] A. J. Larkoski, S. Marzani, G. Soyez, and J. Thaler, "Soft Drop", *JHEP* **05** (2014) 146, doi:10.1007/JHEP05(2014)146, arXiv:1402.2657.

[42] G. Cowan, K. Cranmer, E. Gross, and O. Vitells, "Asymptotic formulae for likelihood-based tests of new physics", *Eur. Phys. J.* **C71** (2011) 1554, doi:10.1140/epjc/s10052-011-1554-0,10.1140/epjc/s10052-013-2501-z, arXiv:1007.1727. [Erratum: Eur. Phys. J.C73,2501(2013)].

[43] P. C. Hansen, "The L-curve and its use in the numerical treatment of inverse problems",.

[44] M. Grazzini, A. Ilnicka, M. Spira, and M. Wiesemann, "Effective Field Theory for Higgs properties parametrisation: the transverse momentum spectrum case", in *52nd Rencontres de Moriond on QCD and High Energy Interactions (Moriond QCD 2017) La Thuile, Italy, March 25-April 1, 2017*. 2017. arXiv:1705.05143.

[45] A. Banfi, P. F. Monni, and G. Zanderighi, "Quark masses in Higgs production with a jet veto", *JHEP* **01** (2014) 097, doi:10.1007/JHEP01(2014)097, arXiv:1308.4634.

[46] G. Bozzi, S. Catani, D. de Florian, and M. Grazzini, "The q(T) spectrum of the Higgs boson at the LHC in QCD perturbation theory", *Phys. Lett.* **B564** (2003) 65–72, doi:10.1016/S0370-2693(03)00656-7, arXiv:hep-ph/0302104.

[47] T. Becher and M. Neubert, "Drell-Yan Production at Small q_T, Transverse Parton Distributions and the Collinear Anomaly", *Eur. Phys. J.* **C71** (2011) 1665, doi:10.1140/epjc/s10052-011-1665-7, arXiv:1007.4005.

[48] P. F. Monni, E. Re, and P. Torrielli, "Higgs Transverse-Momentum Resummation in Direct Space", *Phys. Rev. Lett.* **116** (2016), no. 24, 242001, doi:10.1103/PhysRevLett.116.242001, arXiv:1604.02191.

[49] LHC Higgs Cross Section Working Group Collaboration, "Handbook of LHC Higgs Cross Sections: 4. Deciphering the Nature of the Higgs Sector", `doi:10.23731/CYRM-2017-002,arXiv:1610.07922`.

[50] M. Grazzini. Private communication.

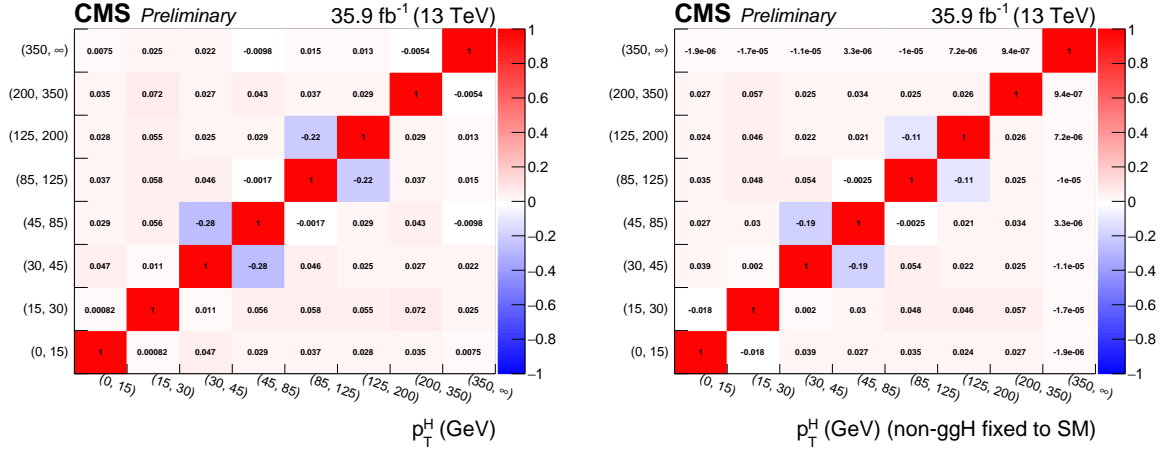## A Correlation matrices for the combinations of differential observables

Figure 11: (left) Bin-to-bin correlation matrix of the p_T^H-spectrum. (right) Bin-to-bin correlation matrix of the p_T^H-spectrum, while keeping the non-gluon-fusion contributions (xH) fixed to SM expectation.
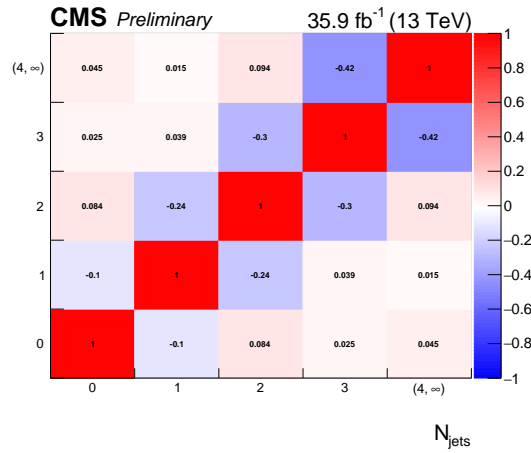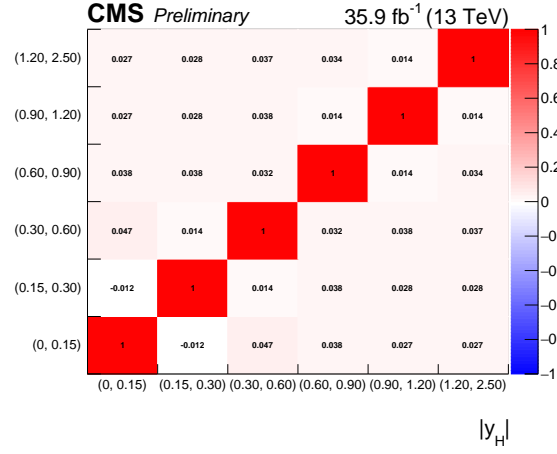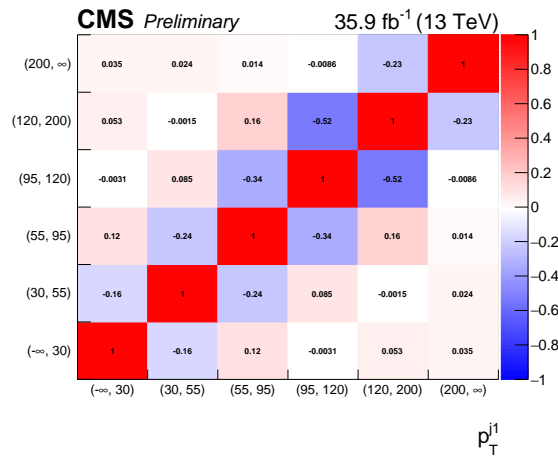

Figure 12: Bin-to-bin correlation matrix of the N_{jets}-spectrum.

Figure 13: Bin-to-bin correlation matrix of the $|y_H|$-spectrum.

Figure 14: Bin-to-bin correlation matrix of the p_T^{jet}-spectrum.